Acta Materialia 296 (2025) 121221

Contents lists available at ScienceDirect

Acta Materialia

journal homepage: www.elsevier.com/locate/actamat

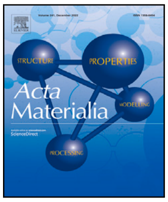

Full length article

Segregation and ordering of light interstitials (B, C, H, and N) in Cr–Ni alloys: Implications for grain boundary stability in superalloy design

Tyler D. Doležal [a,b,*], Rodrigo Freitas [a,**], Ju Li [a,c,**]

[a] Department of Materials Science and Engineering, Massachusetts Institute of Technology, Cambridge, MA, USA
[b] Department of Engineering Physics, Air Force Institute of Technology, Wright-Patterson Air Force Base, OH, USA
[c] Department of Nuclear Science and Engineering, Massachusetts Institute of Technology, Cambridge, MA, USA

ARTICLE INFO

Dataset link: https://github.com/tylerdolezal/hybrid_MCMD, https://github.com/tylerdolezal

Keywords:
Light interstitials
Ni-based superalloys
High-temperature materials
Carbides
Borides
Nitrides
Hydrides
Grain boundaries

ABSTRACT

The segregation and ordering behavior of light interstitials (B, C, and N) in $Cr_{30}Ni$ is examined as these elements are critical for grain boundary (GB) stability and high-temperature mechanical performance in Ni-based superalloys. Using Monte Carlo simulations, we identify the chemical and structural preferences of these interstitials in both bulk and GB environments, aligning with experimental segregation and precipitation trends. Boron strongly prefers GBs over the bulk, where it enhances GB cohesion and stabilizes the GB structure. Uniquely, boron induces a structural transformation at higher concentrations, hinting at the formation of serrated GBs where boron content is high, which improves high-temperature mechanical performance. Carbon and nitrogen form carbide- and nitride-like motifs and exhibit limited GB solubility, reinforcing their precipitation tendencies. In support of ongoing hydrogen embrittlement mitigation strategies, we also examined hydrogen behavior. Hydrogen demonstrated chemical stability in the CrNi GB zone, suggesting it may preferentially migrate inward along Cr- and Ni-rich GBs while avoiding Mo-enriched regions, further supporting Mo's role in mitigating embrittlement. These findings suggest that Mo-containing borides may serve as effective barriers against hydrogen-induced degradation by inhibiting H ingress and stabilizing GB cohesion. By elucidating the chemical and structural preferences of these light interstitials, this work provides a robust computational framework for guiding superalloy design toward improved high-temperature grain boundary stability, resistance to hydrogen embrittlement, and controlled chemical ordering.

1. Introduction

Nickel-based superalloys are indispensable for high-temperature applications due to their remarkable mechanical strength, thermal stability, and resistance to oxidation and creep. These properties are critical for demanding environments in aerospace propulsion, energy generation, and advanced manufacturing. However, several studies have highlighted limitations in these materials. For example, Hosseini and Popovich [1] provided a comprehensive review of the mechanical properties of additively manufactured Inconel 718, identifying challenges such as porosity, anisotropy, and microstructural heterogeneity, which stem from the additive manufacturing process itself. These issues introduce residual stresses and defects that degrade tensile strength, fatigue life, and creep resistance. Jia and Gu [2] demonstrated that selective laser melting (SLM) of Inconel 718 improves microstructure and densification when processed under optimal laser parameters, enhancing microhardness, wear resistance, and oxidation resistance through refined architectures and the formation of protective Cr_2O_3 layers. Similarly, De Souza et al. [3] reviewed welding and additive manufacturing challenges in nickel-based superalloys, emphasizing hydrogen embrittlement (HE) as a significant issue. Their study detailed how welding parameters and post-weld treatments influence hydrogen uptake and subsequent embrittlement, particularly in the heat-affected zone.

In operational environments, prolonged exposure to extreme temperatures exacerbates material degradation. Hardy et al. [4] highlighted the challenges of grain boundary weakening and coarsening of γ' and γ'' strengthening phases during extended high-temperature service, which significantly reduce creep resistance and tensile strength. Khalid and Mansoor [5] explored HE in Inconel 718, identifying weak sites such as δ-phase interfaces and grain boundaries that are prone to decohesion and crack initiation. Their study emphasized the role of hydrogen-enhanced localized plasticity (HELP) and hydrogen-enhanced

---

[*] Corresponding author at: Department of Materials Science and Engineering, Massachusetts Institute of Technology, Cambridge, MA, USA.
[**] Corresponding authors.

E-mail addresses: tyler.dolezal.1@us.af.mil (T.D. Doležal), rodrigof@mit.edu (R. Freitas), liju@mit.edu (J. Li).

https://doi.org/10.1016/j.actamat.2025.121221
Received 27 March 2025; Received in revised form 10 May 2025; Accepted 5 June 2025

decohesion (HEDE) in accelerating embrittlement, with nanovoid nucleation at dislocation slip bands and intergranular decohesion identified as critical mechanisms. Feng et al. [6] investigated the impact of hydrogen on the fracture mechanism of wire arc additive-manufactured Inconel 625, demonstrating a transition from ductile microvoid coalescence to brittle quasi-cleavage, with preferential cracking observed at γ-matrix/Laves phase interfaces. While hydrogen enrichment weakened interface binding forces, the strong hydrogen capture ability of the Laves phase limited segregation at the interface. Baek et al. [7] demonstrated that ultrasonic nanocrystal surface modification (UNSM) mitigates HE in additively manufactured Inconel 625 by refining surface grains, inducing compressive residual stresses, and reducing hydrogen diffusion, resulting in a 6.3% improvement in elongation. Fu et al. [8] and Xu et al. [9] analyzed hydrogen's impact on fatigue crack propagation, finding that it accelerates crack growth and alters microstructural deformation behavior. Lee et al. [10] investigated hydrogen-assisted failure in laser powder bed fused Inconel 718, demonstrating that direct aging (DA) exacerbates embrittlement due to intergranular cracking, while homogenization and aging (HA) mitigates hydrogen susceptibility by reducing trapping and promoting uniform distribution of strengthening phases. Recently, there has been growing interest in investigating the effects of light interstitial elements, such as boron, carbon, and nitrogen, on the properties of nickel-based superalloys.

Boron (B) plays a significant role in enhancing the performance and microstructural integrity of nickel-based superalloys. Antonov et al. [11] highlighted boron segregation at dislocations in additively manufactured superalloys, where it stabilizes dislocation networks and influences grain boundary properties. Kontis et al. [12] showed that boron enhances creep resistance by forming γ' layers at grain boundaries, which impede crack propagation and prevent the formation of continuous $M_{23}C_6$ carbide films. Zhou et al. [13] demonstrated that boron improves stress-rupture life by facilitating dislocation transmission across grain boundaries, dissipating strain, and preventing premature crack initiation. Zhang et al. [14] demonstrated the effectiveness of TiB_2 reinforcements in Inconel 625, improving microhardness by forming Ti- and Mo-rich interfacial layers that enhance mechanical performance. Tian et al. [15] highlighted the synergistic effects of boron and rare earth elements (RE) in strengthening grain boundaries, improving plasticity, and reducing stress concentrations.

Carbon (C) also plays a vital role in strengthening nickel-based superalloys through carbide formation. Tekoglu et al. [16] demonstrated that nanocarbides formed during laser powder bed fusion improve yield and tensile strength by serving as dislocation barriers and enhancing grain refinement. Liu et al. [17] optimized TiC/Inconel 718 composites using a dual-gradient printing strategy, achieving superior mechanical properties through tailored microstructure. Zhao et al. [18] investigated (Nb,Ti)C carbides in composite coatings, revealing their contribution to precipitation stability and hardness. Furthermore, Guan et al. [19] demonstrated that combining boron and carbon in TiB_2-TiC phases significantly enhances mechanical properties, including microhardness and wear resistance, by refining grains and altering wear mechanisms.

Nitrogen (N) contributes to mechanical and tribological properties through nitride formation. Kim et al. [20] showed that TiN coatings improve pitting corrosion resistance in Inconel 600, while Li et al. [21] demonstrated that TiN reinforcements enhance the strength and wear resistance of Inconel 718. However, Lim et al. [22] found that excessive TiN inclusions exacerbate brittle fracture and strain localization, reducing mechanical performance and underscoring the importance of inclusion control in advanced manufacturing processes.

Computational investigations into the behavior of light interstitials in nickel-based systems continue to provide valuable insights. Ji et al. [23] explored the influence of refractory elements (Re, W, Mo, Ta) on B diffusion in nickel-based single crystal superalloys, showing that these elements impede B diffusion. The study identified a trend of decreasing diffusion activation energy (Re < Mo < W < Ta), attributed to differences in atomic radius and hybrid orbital interactions between B and the refractory elements. Rák et al. [24] examined the incorporation of B into nickel ferrite spinel ($NiFe_2O_4$) and revealed that B preferentially forms secondary phases such as B_2O_3, Fe_3BO_5, and $Ni_3B_2O_6$ rather than integrating into the spinel structure, due to the narrow stability domain of nickel ferrite and the high formation energies of B-related defects. Yang et al. [25] focused on the adsorption, absorption, and diffusion of B on Ni (111) surfaces and in bulk Ni, finding that B preferentially adsorbs at HCP-hollow sites on the surface and occupies octahedral interstitial sites within the bulk, with a diffusion barrier of 1.65 eV between neighboring octahedral sites. In a follow-up study, Yang et al. [26] investigated B behavior at grain boundaries (GBs) in Ni. They found that the $\Sigma3(111)[\bar{1}10]$ GB accelerates B diffusion but resists absorption due to its close-packed structure, while the $\Sigma5(210)[001]$ GB, with its larger cavities, acts as an effective trap for B, significantly hindering its diffusion. Yu et al. [27] examined hydrogen solubility and its embrittlement effects at Ni/$Cr_{23}C_6$ interfaces, finding that hydrogen accumulates at octahedral interstitial sites on the Ni side, reducing interface strength and increasing susceptibility to brittle fracture. Similarly, Hu et al. [28] conducted a systematic study on the solubility and mobility of B, C, and N in various transition metals (TMs). They observed that interstitial formation energies follow a periodic trend governed by the interplay between unit cell volume and d-shell electron filling, with octahedral interstitial sites being energetically favorable for all three elements. David et al. [29] further explored the solubility and diffusion of interstitial atoms (H, C, N, and O) in nickel. Their study confirmed that octahedral sites are the most stable positions, while tetrahedral sites exhibit higher elastic instability. Interestingly, C and N atoms showed additional stability at “M” sites, located between octahedral and tetrahedral positions, with temperature effects influencing solubility but having a minimal impact on migration energies.

This study advances the atomistic understanding of light interstitial behavior in nickel-based systems by examining the effects of B, C, H, and N at varying concentrations (1 at.% to 20 at.%). Unlike prior computational studies that primarily focused on pure nickel systems and limited dopant concentrations, this work investigates the $Cr_{30}Ni$ system, a representative model of a basic nickel superalloy composition, to explore the interplay between Ni and Cr in influencing interstitial behavior at a broad range of dopant levels. The analysis considers microstructural geometry and ordering in the pristine face-centered cubic (FCC) lattice as well as in the presence of GBs, offering a comprehensive view of interstitial effects in both bulk and defected environments. By systematically exploring multiple light interstitial types and concentrations within a binary alloy system, this work provides new insights into how compositional complexity and interstitial content influence structural stability and atomic-scale interactions.

2. Methods

2.1. Preparing the bulk structures

2.1.1. Pristine simulation cells

The bulk structures were initialized in an undoped $Fm\bar{3}m$ cubic crystal system consisting of 6 × 6 × 6 conventional FCC unit cells, totaling 864 lattice positions. The supercell was compositionally randomized by distributing Ni and Cr atoms to achieve an overall composition of 30 atomic percent (at%) Cr and 70 at.% Ni ($Cr_{30}Ni$). Doped simulation cells were generated by randomly introducing light interstitials (B, C, H, or N) into the $Cr_{30}Ni$ supercell. The interstitial concentration was systematically varied from 1 at.% to 20 at.%, with increments of 2 at.% up to 10 at.%, followed by a direct increase to 20 at.% to evaluate the system near a more extreme doping concentration.

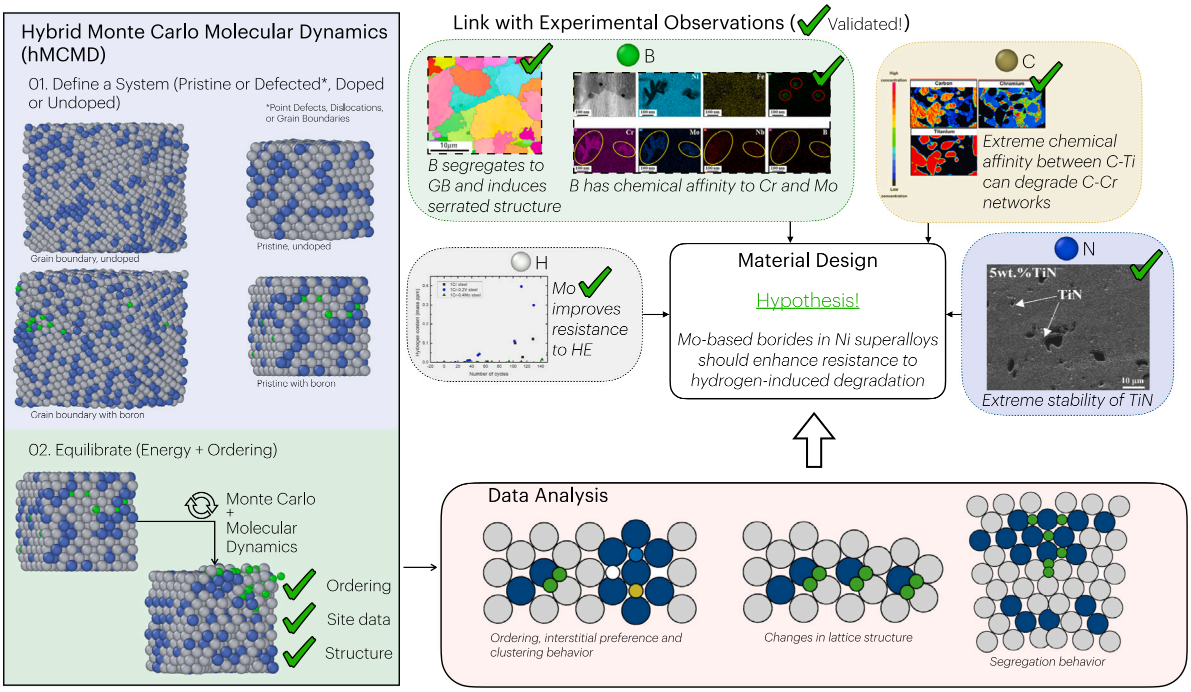

Fig. 1. Schematic representation of the simulation workflow, some interesting topics that are explored, and experimental validation. The hybrid Monte Carlo Molecular Dynamics (hMCMD) approach is used to equilibrate atomic configurations and extract meaningful trends in ordering, interstitial site preference, and segregation behavior. The analysis phase includes clustering behavior and short-range order (SRO), and structural transformations. Several experimental observations are in agreement with our findings, such as boron segregation to grain boundaries, its chemical affinity for Cr and Mo, and how C–Ti interactions disrupt C–Cr networks. Experimental observations compiled from B [30], C [31], H [32], and N [21]. Finally, we propose a hypothesis that Mo-based borides in Ni superalloys could enhance resistance to hydrogen-induced degradation, inviting further experimental validation.

2.1.2. Grain boundary simulation cells

To investigate the impact of GBs, a single GB was introduced into the center of a randomly populated pristine $Cr_{30}Ni$ FCC supercell consisting of 5,321 lattice positions. The GB simulation cell had dimensions of (39.52, 39.52, 39.52) Å. The GB was introduced with a random orientation using Atomsk [33] and fifteen distinct, undoped, GB simulation cells were generated and relaxed to determine the GB energy (γ_{GB}). The GB energy was determined using Eq. (1):

$$\gamma_{GB}(T=0) = \frac{E_{GB} - N(E_0/N_0)}{2A_{GB}}, \tag{1}$$

where E_{GB} is the energy of the GB simulation cell, N is the number of atoms in the GB simulation cell, E_0 is the energy of the pristine structure, N_0 is the number of atoms in the pristine structure, and A_{GB} is the area of the GB (add a factor of 2 to account for a PBC GB). The complete relaxation scheme was a conjugate gradient (CG) structural relaxation with an energy and force convergence criteria of 1×10^{-6} and 1×10^{-8}, respectively, followed by a canonical (NVT) molecular dynamics (MD) simulation for 5 ps at 1000 K, followed by CG structural relaxation with an energy and force convergence criteria of 1×10^{-12}. This was performed using the Large-scale Atomic/Molecular Massively Parallel Simulator (LAMMPS) software [34] and version 5.0.0 of the universal core neural network Preferred Potential (PFP) [35] with the D3 correction implemented through Matlantis [36]. The configuration with the lowest γ_{GB} was selected for further analysis. The GB energy of the selected undoped $Cr_{30}Ni$ system was γ_{GB} = 0.800 J/m^2, which is in good agreement with the range of experimentally measured and computationally predicted GB energies for Ni [37,38]. Doped variations of the GB supercell were generated by randomly introducing light interstitials (B, C, H, or N) into the undoped GB structure up to 4 at.%.

2.2. Computational details

The Monte Carlo (MC) simulations were performed on both the undoped and doped $Cr_{30}Ni$ systems, with five independent runs for each light interstitial concentration in the pristine systems. Each run was initialized from a randomized atomic configuration to ensure independent sampling and to minimize the risk of entrapment in local energy basins. Reported results include error bars representing the variability across the five MC runs. For the GB systems, only a single MC simulation was conducted per light interstitial concentration. This approach was informed by preliminary GB simulations which exhibited minimal statistical variability due to the significantly larger number of atoms and GB segregation in the GB simulation cells. Simulations were set to run until thorough equilibration was achieved in both the energy and short-range ordering of the systems. The MC algorithm trialed the following moves:

1. **Swap atomic positions of metallic constituents:** Select two metallic atoms of different chemical types and attempt to swap their positions within the lattice.
2. **Relocate a light interstitial atom near a new metallic host:** Select a light interstitial atom and attempt to place it near a different metallic atom within its nearest neighbor shell.
3. **Introduce proximity between two light interstitial atoms:** Select two light interstitial atoms and attempt to place one of them within the first nearest neighbor shell of the other. If the first shell is fully occupied, the placement is attempted in the second nearest neighbor shell.
4. **Separate two neighboring light interstitial atoms:** If a pair of neighboring light interstitials exists, select one and attempt to move it away from its nearest interstitial neighbor. This move balances the proximity adjustment, ensuring an opportunity to promote both segregation and aggregation of light interstitials.
5. **Swap a metal neighbor of a light interstitial atom:** For a selected light interstitial atom, identify one of its nearest metallic neighbors and swap its position with that of another metal atom of a different chemical type.

These moves were designed to explore the configurational space of the system effectively, balancing local aggregation and dispersion tendencies of the light interstitial atoms within the metallic matrix. Nearest neighbors were located within a cutoff radius of 2.75 Å. The move was accepted or rejected based on the potential energy difference between the final and initial states, following the Metropolis criterion [39]. The probability of acceptance is expressed as a Boltzmann probability:

$$P(\Delta U) = \min\{1, e^{-\Delta U/k_B T_{\text{sim}}}\}, \tag{2}$$

where ΔU is the potential energy difference between the final and initial states, k_B is the Boltzmann constant in eV/K, and T_{sim} is the simulation temperature in K, which was set to 1073 K (800°C) for this work. For the MC simulations on the undoped $Cr_{30}Ni$ system, only the first move was trialed. The potential energy difference for each trial was calculated using LAMMPS, with structural relaxation performed via the CG method with an energy and force convergence criterion of 1×10^{-12}. The simulations were executed using version 5.0.0 of the universal core neural network PFP with the D3 correction implemented through Matlantis. Matlantis has been shown to be suitable for the modeling of Ni-based superalloys and their interactions with light interstitials [40–44]. The MC-equilibrated GB structures underwent a final NVT MD simulation at 1073 K for 5 ps, followed by CG relaxation with energy and force convergence criteria of 1×10^{-12}.

2.3. Analysis methods

2.3.1. Atomic ordering and structure

The Warren-Cowley short-range order (SRO) parameter (α_{ij}) [45, 46] was examined to quantify the degree of atomic ordering in the system. The SRO parameter is defined as:

$$\alpha_{ij}(r) = 1 - \frac{P_{ij}(r)}{c_j}, \tag{3}$$

where $P_{ij}(r)$ is the probability of finding atom j as a neighbor to atom i at a distance r, and c_j is the atomic fraction of species j. This parameter was calculated for interstitial-metal (i-M) and metal–metal (M-M') pairs across varying light interstitial types (B, C, H, and N) and concentrations. The results were averaged over the five independent MC simulations for each system to improve statistical reliability. By analyzing α_{ij} as a function of light interstitial type and concentration, the study provides insight into the aggregation or segregation tendencies between alloy constituents, revealing how the presence and amount of light interstitials influence local atomic ordering.

Changes in the crystal structure were examined using polyhedral template matching (PTM) [47] as implemented in the OVITO Python API [48]. This method allowed for the identification of local atomic environments by comparing the surrounding atomic arrangements to ideal polyhedral templates. For this analysis, light interstitial atoms were removed from the lattice to isolate and examine the spatial arrangement of the remaining metallic constituents. The PTM analysis was conducted as a function of the light interstitial type (B, C, H, or N) and concentration. This approach provides insights into how the presence and content of light interstitials affect the underlying crystal structure of the binary matrix.

2.3.2. Excess energy

The excess energy (E_{excess}) was calculated as a function of light interstitial using Eq. (4):

$$E_{\text{excess}}^{(i)} = \frac{E_{\text{doped}}^{(i)} - N_m\left(\frac{E_0}{N_0}\right) - N_i E_i}{N_m + N_i}, \tag{4}$$

where $E_{\text{doped}}^{(i)}$ is the averaged total energy of the simulation cell doped with interstitial species i, N_m is the number of metal atoms in the doped simulation cell, N_i is the number of light interstitials of species i in the doped simulation cell, E_0 is the energy of the undoped simulation cell, and N_0 is the total number of atoms in the undoped cell. The term E_i represents the chemical potential energy of the interstitial species derived from a reference state, which serves as a baseline for determining the relative energetic stability of the dopant within the alloy matrix. The excess energy is a measure of how favorable it is for B, C, H or N to remain in the MC equilibrated binary metal environment versus leaving to form a more preferred ordering.

Table 1
Reference compound data and computed interstitial chemical potential energies (E_i) as defined in Eq. (5).

Boron (B)			**Carbon (C)**		
Compound	Space Group	E_i (eV/atom)	Compound	Space Group	E_i (eV/atom)
CrB	$I4_1/amd$	–7.619	$Cr_{23}C_6$	$Fm\bar{3}m$	–8.604
FeB	Cmcm	–7.313	$Fe_{23}C_6$	$Fm\bar{3}m$	–8.073
MoB	$I4_1/amd$	–7.525	Mo_2C	Pbcn	–8.380
NbB	Cmcm	–8.054	Nb_2C	Pnma	–9.354
NiB	Cmcm	–7.026	Ni_3C	$R\bar{3}c$	–7.776
TiB_2	P6/mmm	–8.159	Ti_2C	$Fd\bar{3}m$	–9.963
Hydrogen (H)			**Nitrogen (N)**		
Compound	Space Group	E_i (eV/atom)	Compound	Space Group	E_i (eV/atom)
CrH	$Fm\bar{3}m$	–2.380	Cr_2N	$P\bar{3}1\ m$	–6.645
FeH	$Fm\bar{3}m$	–2.339	Fe_3N	$P6_322$	–5.769
MoH	$P6_3/mmc$	–1.355	MoN	$P6_3mc$	–6.122
NbH_2	$Fm\bar{3}m$	–2.720	Nb_2N	$P\bar{3}1\ m$	–8.007
NiH	$Fm\bar{3}m$	–2.434	Ni_3N	$P6_322$	–5.241
TiH_2	I4/mmm	–3.127	TiN	$Fm\bar{3}m$	–9.004

The selection of reference states for interstitial chemical potential energy calculations is important in ensuring physically meaningful comparisons. Given that Ni-based superalloys commonly contain Ni, Cr, Fe, Mo, Nb and Ti, the energetic contributions of interstitial species (B, C, H, and N) were extracted from binary compounds with Ni, Cr, Fe, Mo, Nb and Ti. The compounds were compiled using Materials Project [49] and the compound with the lowest formation energy was used. The full data set is included in the Supplemental Materials (Tables S1 and S2). To obtain E_i, the relaxed total energy of the reference state was computed, and the interstitial chemical potential energy per atom was determined from Eq. (5):

$$E_i = \frac{E_{\text{comp}} - N_m\left(\frac{E_{\text{metal}}}{N_{\text{metal}}}\right)}{N_i}, \tag{5}$$

where E_{comp} is the total energy of the reference boride, carbide, hydride, or nitride compound, E_{metal} is the total energy of the corresponding bulk metal system, and N_{metal} is the number of metal atoms in the bulk metal system. In Eq. (5), N_m and N_i represent the number of metal and interstitial atoms in the compound, respectively. The extracted interstitial energies and reference compound data are given in Table 1. By using these reference states, the calculated E_{excess} values more accurately capture the thermodynamic tendencies of B, C, H, and N in their preferred short-range ordered configurations. This approach ensures that E_{excess} reflects the balance between interstitial dissolution and clustering within the alloy, while also enabling direct comparisons between different B–M, C–M, H–M, and N–M interactions. Importantly, the selected reference phases are not used to predict phase formation. Rather, they serve as consistent thermodynamic anchors to evaluate the relative chemical driving forces for interstitial ordering with various members of the Inconel metallic constituents.

Systematically comparing E_{excess} across different reference compounds and interstitial types provides valuable insight into the thermodynamic preferences and chemical behavior of these species within the Ni-based superalloy environment. A negative E_{excess} ($E_{\text{excess}} < 0$) for a given interstitial with respect to a specific reference compound suggests that, within the chemically complex Cr–Ni matrix, the interstitial is thermodynamically stabilized through its finalized ordering. In contrast, a positive E_{excess} ($E_{\text{excess}} > 0$) indicates that, despite having access to its preferred local ordering within the MC-equilibrated

Cr–Ni system, the interstitial would still be more stable in a region enriched in the reference metal species (e.g., Cr or Ti). For example, a positive E_{excess} for B with respect to Cr–B ordering implies that B would prefer a more Cr-rich environment than is available in the Cr–Ni alloy matrix. Similarly, comparing E_{excess} among B, C, H, and N enables evaluation of which interstitials are more likely to remain in solution versus contribute to chemical clustering. These calculations provide a thermodynamic framework for interpreting interstitial site preferences, segregation tendencies, and their potential influence on alloy microstructure and properties.

2.3.3. Grain boundary energetics and geometry

The GB energy of the doped GB structures ($\gamma_{\text{GB}}^{(\text{doped})}$) was computed according to Eq. (1) with the exception that it must account for the energy differences between the doped GB and pristine structures, i.e., $E_{\text{GB}} \rightarrow E_{\text{GB}}^{(\text{doped})}$ and $E_0 \rightarrow E_0^{(\text{doped})}$. This analysis used the doped, MC equilibrated, structures to evaluate the stability of interstitial species (B, C, H, N) as a function of content. A decrease in $\gamma_{\text{GB}}^{(\text{doped})}$ with increasing interstitial content indicates a stabilization effect. Additionally, segregation energy (E_{seg}) for the different interstitials as a function of content was determined as defined in Eq. (6) [50]:

$$E_{\text{seg}}^{(i)} = \left(\frac{E_{\text{GB}}^{(i)}}{N_{\text{GB}}} - \frac{E_{\text{bulk}}^{(i)}}{N_{\text{bulk}}} \right) - \left(\frac{E_{\text{GB}}^{\text{undoped}}}{N_{\text{GB}}^{\text{undoped}}} - \frac{E_{\text{bulk}}^{\text{undoped}}}{N_{\text{bulk}}^{\text{undoped}}} \right), \tag{6}$$

where $E_{\text{GB}}^{(i)}$ and N_{GB} represent the total energy and number of atoms in the GB system (doped with interstitial i), respectively. The terms $E_{\text{bulk}}^{(i)}$ and N_{bulk} represent the total energy and number of atoms in the pristine system (doped with interstitial i), respectively. The terms $E_{\text{GB}}^{\text{undoped}}$ and $N_{\text{GB}}^{\text{undoped}}$ represent the total energy and number of atoms in the undoped GB system, respectively. The terms $E_{\text{bulk}}^{\text{undoped}}$ and $N_{\text{bulk}}^{\text{undoped}}$ represent the total energy and number of atoms in the undoped pristine system, respectively. This expression accounts for the energy difference between the doped and undoped GB systems, normalized per atom, and subtracts the corresponding energy difference for the pristine systems. The resulting E_{seg} value indicates the relative stability of the light interstitial at the GB compared to its bulk solubility. Where $E_{\text{seg}} < 0$ indicates segregation is favorable and $E_{\text{seg}} > 0$ indicates segregation is unfavorable.

To assess changes in GB morphology, the relative free volume of metallic atoms (Cr and Ni) within the GB region was calculated as a function of interstitial type and concentration. For each metallic atom in the GB, the relative free volume ($\tilde{V}$) was defined as:

$$\tilde{V}_j = \frac{V_{j,\text{GB}} - \langle V_{\text{bulk}} \rangle}{\langle V_{\text{bulk}} \rangle}, \tag{7}$$

where $V_{j,\text{GB}}$ is the atomic volume of metal atom j in the GB, and $\langle V_{\text{bulk}} \rangle$ is the average atomic volume derived from the 5 equilibrated undoped pristine $Cr_{30}Ni$ structures. Using the compiled $\tilde{V}$ values, the mean (μ) and standard deviation ((σ) of the relative free volume across all metallic atoms within the GB zone was recorded. To quantify the smoothness of the GB plane, the root mean square (RMS) roughness (R_q) was computed using Eq. (8):

$$R_q = \sqrt{\frac{1}{N_m} \sum_{j=1}^{N_m} (z_j - \bar{z})^2}, \tag{8}$$

where z_i is the height of the jth metallic atom, $\bar{z}$ is the mean height of atoms within the GB region, and N_m is the total number of metallic atoms present in the GB zone. This quantity represents the degree of vertical variability or deviation of GB atomic positions from the average GB plane, with larger values of R_q indicating greater surface roughness. To clearly illustrate how the light interstitials impact R_q, the absolute difference between the doped and undoped systems was taken,

$$\tilde{R}_q = R_q^{(i)} - R_q^{(\text{undoped})}, \tag{9}$$

where negative values of $\tilde{R}_q$ represent a flatter GB plane and positive values correspond to increased roughness compared to the undoped GB plane. These geometric measures are summarized in Table 2.

3. Results and discussion

3.1. Atomic ordering and structure

The Warren-Cowley SRO parameters (α_{ij}), as defined in Eq. (3), are presented in Fig. 2a for interstitial-Cr (blue), interstitial-Ni (orange), Cr–Cr (green), Cr–Ni (red), and Ni–Ni (purple) as a function of interstitial content for B, C, H, and N. These values were extracted from five independent MC equilibrated simulations, and the error bars represent the variability between these runs. To contextualize these ordering trends, the corresponding structural types are shown in Fig. 2b, with cluster configurations provided in Fig. 2c. Boron predominantly formed B_2 in the tetrahedral interstitial site, while C, H, and N preferentially occupied the octahedral interstitial site.

Across all interstitials, C and N exhibited the strongest affinity for Cr, as indicated by the consistently negative α_{CCr} and α_{NCr} values. However, their behavior diverged at higher concentrations due to differences in carbide and nitride motif formation. The α_{CCr} value initially exhibited a strong negative trend but gradually increased with increasing C content, suggesting that C reached a saturation point with Cr, limiting further clustering. This behavior aligns with carbide stoichiometry, where a single C atom is typically coordinated by multiple Cr atoms (e.g., $Cr_{23}C_6$), leading to a depletion of available Cr neighbors at high C concentrations. In contrast, α_{NCr} remained consistently negative across N content, indicating that N continued clustering with Cr without experiencing the same saturation constraints. This is likely due to the balanced Cr:N ratio in nitride formation (e.g., CN), allowing N to maintain strong Cr affinity even at higher concentrations. Meanwhile, B exhibited negative α_{BCr} and α_{BNi} values, with an affinity for Cr over Ni. The B-(Cr, Ni) interactions fluctuated significantly at 1 and 2 at.% B concentrations, but stabilized beyond 4 at%, which coincided with the beginning of a structural transformation (Fig. 2b). Unlike C, H, and N, which influenced local chemical ordering with little or no structural impact, B actively contributed to structural rearrangement. This effect was evident in the decreases in α_{CrCr} and α_{NiNi}, indicating a structurally induced disruption to M-M' ordering. Similar to B, H showed a preference to cluster with both Cr and Ni, but more evenly. Because of this, H had a stronger effect on Cr–Ni interactions, reducing α_{CrNi} more than any other interstitial, indicating that H modified Cr–Ni ordering more effectively. Overall, these trends highlight distinct interstitial behaviors on local lattice ordering: C and N exhibited the strongest affinity for Cr, but C reached a saturation limit, whereas N maintained clustering across all concentrations. B was the most disruptive to the overall structure, while both B and H had similar preferences on chemical ordering. These insights provide an interesting understanding of how different light interstitials modify Cr–Ni systems, with implications for chemical stability and early-stage microstructural evolution.

Recent experimental work [51] examined the impact of C and H in the octahedral interstitial site on Ni microstructure. Their findings confirmed that both C and H preferentially occupy octahedral sites, supporting the site preferences observed in this study. Additionally, they reported that interstitial C inhibited unwanted hydrogenation, further highlighting its role in modifying Ni's chemical environment. This aligns with the well-established tendency of Cr and C to form large-scale carbide networks with complex morphologies [52–54], further reinforcing the observed preference for extensive C–Cr clustering.

Recent first-principles calculations support site preference and ordering observed here, demonstrating that C and N favor octahedral interstitial sites in FCC metals, whereas B exhibits different behavior, with a higher formation energy and migration barrier [28], which may

Table 2
Atomic fraction of the interstitial in the GB region ($x_{\mathrm{GB}}^{(i)}$), mean (μ) and standard deviation (σ) of the relative free volume ($\tilde{V}$, defined in Eq. (7)) for only the *metallic atoms* (Cr, Ni) in the GB region, as well as the absolute difference in RMS roughness ($\tilde{R}_q$, defined in Eq. (8) and Eq. (9)) for the equilibrated GB cell at total dopant concentrations of 1, 2, and 4 at.%. The undoped equilibrated GB simulation cell values serve as a baseline reference.

Light	$x_{\mathrm{GB}}^{(i)}$ (at%)			μ (%)			σ (%)			$\tilde{R}_q$ (Å)		
Interstitial	1	2	4	1	2	4	1	2	4	1	2	4
B	3.09	9.60	12.2	1.62	0.933	−0.132	4.31	4.55	5.07	−0.249	−0.409	−0.293
C	4.00	6.77	11.8	2.14	1.52	0.922	4.55	4.51	4.68	−0.133	−0.249	−0.197
H	3.10	4.94	10.3	1.91	1.32	−1.18	4.75	4.84	6.09	−0.216	0.583	−0.0486
N	4.62	6.50	9.80	2.20	1.06	1.68	4.31	4.54	4.83	0.115	−0.225	−0.185
Undoped	–			3.20			4.45			2.18		

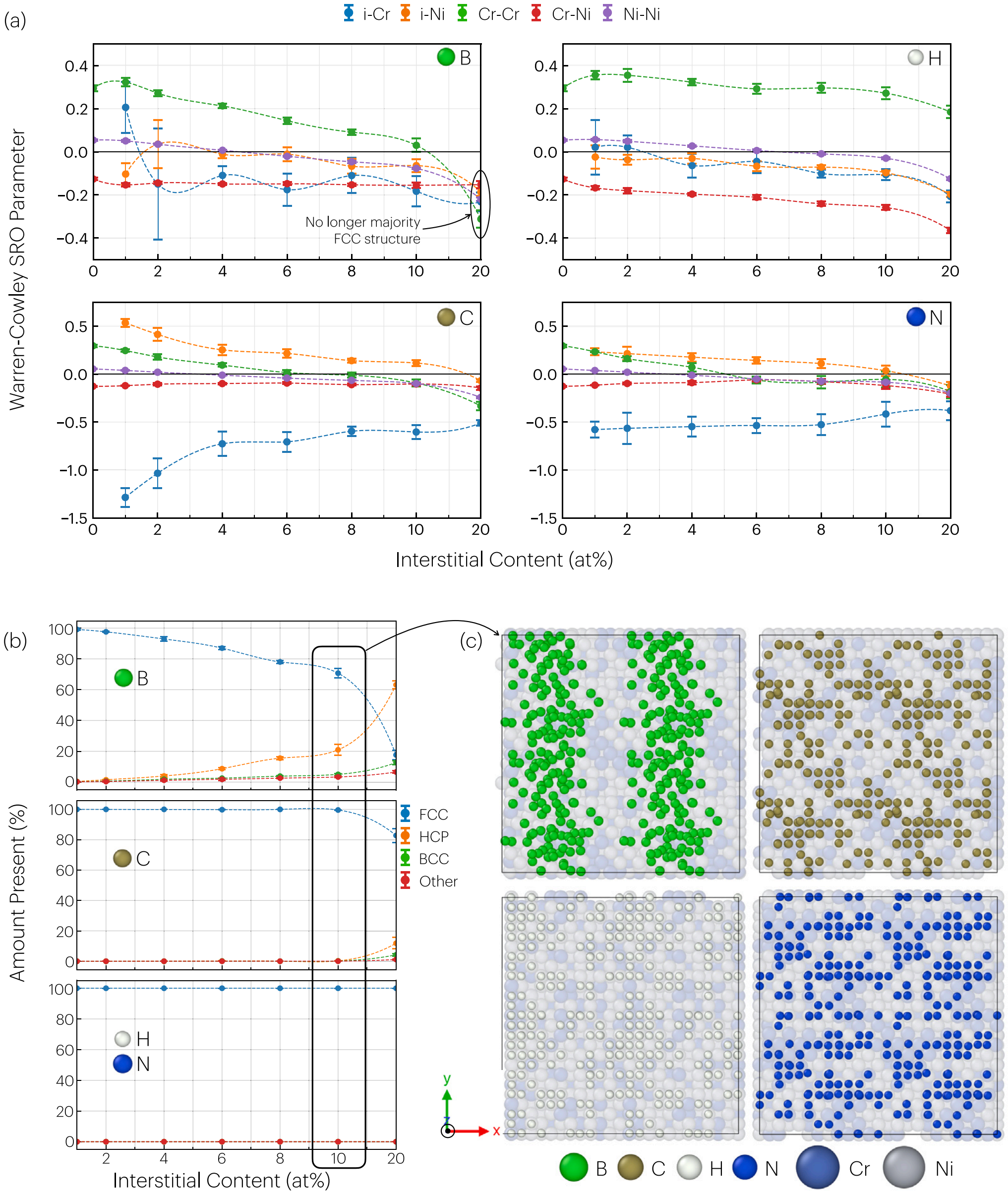

Fig. 2. The (a) short-range order (SRO) parameter, as given in Eq. (3), for the interstitial-metal (i-M) and metal–metal (M-M') pairs and (b) structure type in the pristine $Cr_{30}Ni$ supercell shown as a function of interstitial type and content. A single graph is shown for hydrogen or nitrogen, as their graphs were identical. (c) A final structure, replicated using a (2, 2, 1) supercell expansion to highlight clustering across the simulation cell boundaries.

contribute to its localized clustering behavior. Additionally, the solubility and migration behavior of these elements follow periodic trends, with C exhibiting lower formation energies and higher mobility compared to B and N, potentially driving its stronger clustering tendencies. Further insight into interstitial site preferences and diffusion mechanisms is provided by density functional theory (DFT) calculations [29] which confirmed that C and N preferentially occupy octahedral sites. The charge transfer analysis showed that C and N strongly interacted with neighboring Ni atoms, while H exhibited weak Ni interactions, supporting its reduced clustering tendency.

The shared ordering observed between C and N with Cr suggests the potential for synergistic effects, as N has been shown to promote

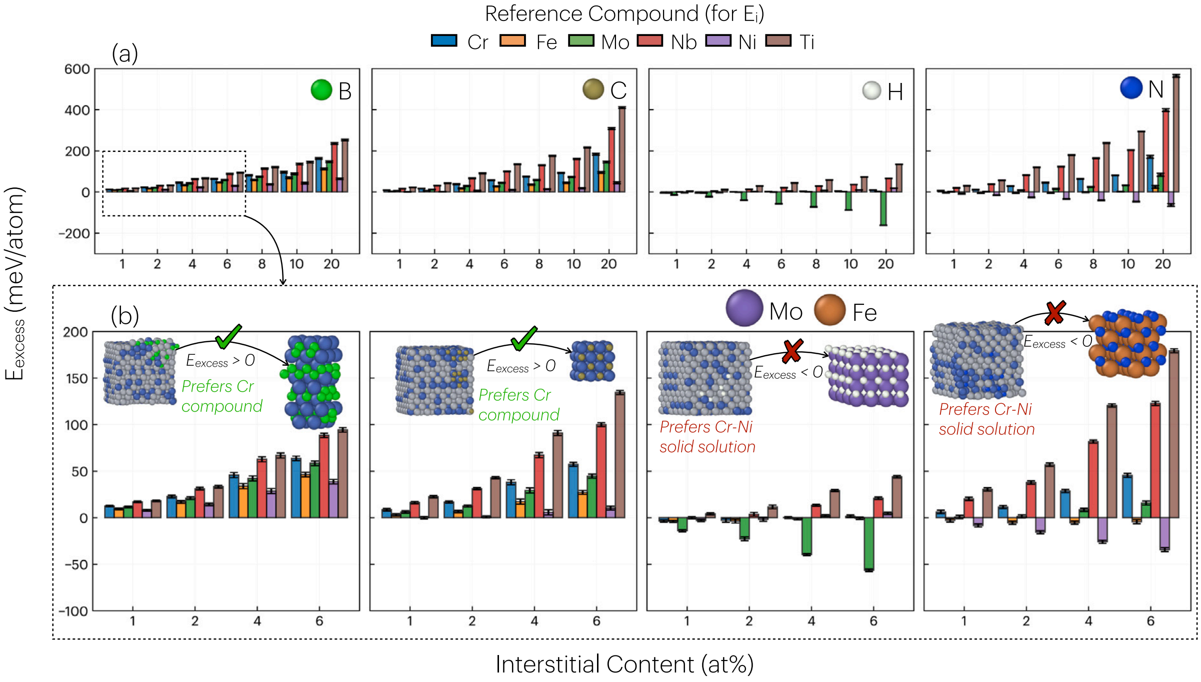

Fig. 3. (a) Excess energy (E_{excess}), as defined in Eq. (4), plotted against interstitial type, concentration, and the reference compound used to calculate E_i (Eq. (5)). (b) A magnified view of E_{excess} for interstitial concentrations of 6 at% or lower, with schematics illustrating key trends and behaviors that E_{excess} helps reveal. The label corresponds to the metal component of each reference compound, e.g., Cr for Cr–i (i = B, C, H, N) or Fe for Fe–i (i = B, C, H, N), etc.

the formation of carbonitrides [55]. Given that both C and N exhibited strong clustering with Cr in these simulations, their co-presence in a system could enhance carbonitride formation. This adds an additional complexity to the idea that interstitial-driven ordering in Ni-based alloys is governed not only by individual solute behaviors but also by their collective interactions with metallic elements. Lastly, B was unique in that it was the only light interstitial to drive a structural transition (see Fig. 2b). This is particularly notable given B's well-known tendency to segregate to GBs and strengthen them by altering GB morphology through induced serrations [12,30,56–58]. Unlike C, N, and H, which maintained the FCC lattice even at high concentrations, B progressively destabilized the FCC phase, ultimately leading to a majority transformation to HCP at 20 at% B content. This drastic structural shift underscores a fundamental difference in how B interacts with the Ni-based matrix compared to other interstitials. The FCC-to-HCP transition supports the common observation that, in regions of high B concentration such as GBs, B can promote local structural transformations. Further investigations were performed on the deformed $Cr_{30}Ni$ B-doped structures. When B atoms were removed and the structures were re-relaxed, the FCC phase was largely restored, with more than 95% of the system reverting to its original structure. However, small perturbations remained, with trace amounts of HCP and 'Other' structural deviations, indicating that while B-induced lattice disruptions are mostly reversible, residual irregularities persist. This suggests that the destabilization arises from a B-driven perturbation rather than a permanent phase transformation. The reversibility highlights the transient nature of B-induced structural disruptions, reinforcing the idea that B acts as a local structure modifier rather than an agent of permanent phase change.

3.2. Excess energy

Fig. 3 presents the calculated excess energy, E_{excess}, for B, C, H, and N as a function of interstitial content. The color of each bar corresponds to the reference compound used to extract E_i, which has been compiled in Table 1. As a reminder, a more positive E_{excess} value indicates a preference for that interstitial to segregate and form the compound/ordering associated with the reference structure, while negative values suggest a tendency to remain within the mixed-metal matrix. Importantly, because the host lattice was equilibrated through MC simulations prior to these calculations, there is a confidence that each light interstitial has reached its preferred ordering and lowest-energy configuration within the $Cr_{30}Ni$ system before being compared to reference compounds.

The most immediate and striking observation is that all light interstitials exhibit a strong preference to segregate with Ti, with C and N showing the highest E_{excess} values. This trend aligns with the well-documented affinity of these elements for Ti, known to form stable borides (TiB_2), carbides (e.g., TiC), hydrides (TiH_2) and nitrides (e.g., TiN) [59–66]. Another key observation is that B exhibits positive excess energy values across all reference structures, even at the lowest concentrations, indicating negligible solubility in the $Cr_{30}Ni$ lattice and a strong chemical affinity for compound-forming elements, as reflected in positive E_{excess} values. This result is in excellent agreement with experimental data for B in both pure Ni and pure Cr at 800 °C, where B readily forms Ni_3B and Cr_2B [67–69]. The presence of Cr does not improve the solubility of B in the Ni matrix, further reinforcing its strong tendency toward segregation and precipitation.

In a typical Ni-based superalloy, such as Inconels, the composition consists primarily of Ni, followed by Cr, Mo, Fe, and small amounts of Ti. If each reference compound in this analysis represents a potential "segregation route" for B, then multiple pathways were available for its escape from the $Cr_{30}Ni$ matrix. Based on the magnitude of E_{excess}, TiB_2 was the most favorable segregation route. However, in a realistic alloy system, the probability of B aggregating enough Ti to precipitate as TiB_2 is low. Instead, B is more likely to encounter Cr, Mo, Fe, and some Nb where it showed a stronger preference for Mo and Nb over Cr and Fe. Thus, if B is introduced into a NiCrMoFeTi mixed-metal system, it should preferentially segregate in regions rich in Nb and Mo rather than in the Ni γ matrix. Given B's known tendency to segregate to GBs, this hypothesis can be refined further: B should be found at GBs where it would aggregate with Nb and Mo. Experimental validation of this hypothesis can be found in Ref. [30,70], which reported ordering of Cr, Mo, Nb, and B in Inconel 625 and Cr, Mo, Nb, and B in Inconel

718, respectively. In these studies, B was introduced via TiB_2 and ZrB_2 doping. In the absence of sufficient Ti, B dissociated and re-ordered with Cr, Mo, and Nb aligning with the E_{excess} analysis.

Recent experimental studies on the partitioning behavior of Mo and Cr in Ni-based superalloys have shown that Cr preferentially partitions to the γ matrix, while Mo's distribution shifts dynamically depending on Cr content [71–74]. It was determined that higher Cr concentrations reduced Mo's solubility in γ' precipitates, driving its redistribution to the γ phase. This redistribution behavior suggests a complex interplay between Cr and Mo, where Cr-rich environments indirectly influence the stability and partitioning tendencies of Mo within the alloy. Given this interplay, the addition of B introduces another layer of complexity. Specifically, B-enriched regions should also be Cr/Mo-rich. Since Mo's solubility in γ' decreases as Cr content rises, B segregation could further reinforce Mo partitioning to the γ matrix, altering the Cr/Mo balance. This suggests that B's presence at GBs may not only influence segregation behavior (and morphology) but also stabilize Cr/Mo-rich GB phases while further depleting Mo from γ'. The interdependence between B segregation and Cr/Mo redistribution highlights a potential avenue for tailoring microstructural properties, warranting further experimental validation.

Transitioning now to C, the excess energy results in Fig. 3b highlights its limited solubility in the $Cr_{30}Ni$ matrix. Compared to pure Ni and pure Cr, where C exhibits practically no solubility at 800 °C [75,76], the addition of Cr has no measurable effect on stabilizing C in solid solution, as expected. This is reflected in the positive E_{excess} values observed across all dopant concentrations, indicating a consistent thermodynamic drive for segregation and compound formation. The negative and low E_{excess} values for NiC suggests that C would remained preferentially clustered with Cr as an interstitial in the Cr–Ni lattice rather than form a Ni-based carbide. It is particularly interesting to observe positive E_{excess} values for the other alloy constituents, with C–Ti and C–Nb displaying the largest positive value. The positive values indicate that these elements serve as favorable segregation routes, despite C achieving strong ordering with Cr in the equilibrated $Cr_{30}Ni$ cell. For Mo, this observation aligns well with ab initio calculations reporting the strong thermodynamic stability of Mo–C [77], as well as experimental work demonstrating the persistence of Mo-based carbides in Ni/Fe Cr–Mo systems [78,79]. Additionally, it supports the recent observations of both Cr and Mo participating in carbide formation at GBs [80] in Ni–Cr–Mo alloys. While Fe-based carbides are energetically favorable, they are not commonly observed in Ni-based systems due to Fe's solubility in the γ matrix. The positive E_{excess} value suggests that Fe–C formation would be preferable over Cr–C *if* Fe were available for carbide formation. However, Fe remains largely stable in solid solution and lacks a significant segregation drive, preventing Fe-based carbides from forming in appreciable amounts.

The chemical affinity between C and Ti is significant considering experimental evidence which supports the competitive interaction between TiC and Cr-based carbides [31,81]. The study from Ref. [31] confirmed that TiC exhibits strong thermodynamic stability and a high melting point, often outcompeting other carbides in metal matrices. In systems containing Cr, TiC influenced carbide formation by altering the solubility and stability of Cr-rich carbides [31,81], consistent with the fact that TiC had the highest E_{excess} among all reference carbides. Additionally, the redistribution of C in TiC-containing systems was shown to impact the dissolution and re-precipitation of $Cr_{23}C_6$ carbides [31] which can weaken GB stability [81]. Together, these findings reinforce the critical role of Ti in disrupting Cr-based carbide stability and highlight its broader implications in Ni-based alloys. The competition between Cr- and Ti-based carbides presents a significant challenge for microstructural stability, especially when doping with TiC [30,31,81], emphasizing the need for careful control of Ti content to mitigate adverse effects on GB cohesion and mechanical performance.

Given the strong affinity between C-Nb, it is important to note how NbC plays a crucial role in carbide formation and GB stabilization in Ni-based alloys. Unlike TiC, which disrupts Cr-rich carbides, NbC primarily increases the overall carbide fraction, forming both within grains and at GBs [82]. The work of Ref. [82] found that Nb-based carbides serve as a strong pinning agent, reducing GB mobility and refining the microstructure, thereby enhancing creep resistance and tensile strength. The work of Li et al. [83] discovered that, as annealing temperature increases, NbC stability decreased relative to Cr-Mo carbides, which lead to a transition in carbide composition from (Nb, Ti)C to (Cr, Mo, W)C. This suggests that NbC and TiC play a dynamic role in carbide phase evolution, influencing long-term microstructural stability in Ni-based alloys. These results underscore the importance of leveraging atomistic insights to capture the fundamental mechanisms governing metal stability in the presence of light interstitials, providing a more detailed understanding of how elemental interactions at the atomic scale influence larger-scale behavior.

Hydrogen is a unique light interstitial to consider due to its well-documented role in degrading mechanical performance. Understanding its preferred ordering with the metallic constituents of Ni-based superalloys may provide atomistic insights into strategies for mitigating deleterious H aggregation within the microstructure. What stands out most with H is its clear avoidance of Mo and its near-neutral interactions with Ni, Cr, and Fe. This behavior suggests that while H does not exhibit a strong driving force to cluster with major alloying elements, its selective repulsion from Mo may have implications for H trapping mechanisms and embrittlement resistance. Recently, experimental studies have demonstrated that Mo-carbides exhibit superior H-trapping capabilities, significantly enhancing resistance to HE [32,84,85]. First-principles calculations further confirm that Mo reduces H solubility in metallic systems, offering greater HE resistance than W [86]. Moreover, Mo_2C carbides have been experimentally shown to serve as effective H traps, lowering H diffusivity and improving HE resistance [87]. Additionally, Ref. [88] demonstrated that Mo-containing carbides improved HE resistance by stabilizing GBs and mitigating H-assisted fracture. These experimental findings align with the segregation trends which indicated repulsion of H from Mo, reinforcing the role of Mo-rich regions as effective H diffusion barriers, potentially reducing embrittlement risks in Ni-based alloys. This highlights the critical role of Mo in both carbide formation and microstructural stability under H exposure, further underscoring its importance in alloy design.

Interestingly, recent experimental work has demonstrated that B, like Mo, enhances HE resistance by segregating to GBs and repelling H [89]. Thermal Desorption Spectroscopy (TDS) measurements indicated that B passivates GBs against H accumulation. Ab initio calculations [89] further confirmed that B has a stronger attraction to GBs than H, suggesting a repulsive interaction that prevents H segregation. Given B's well-documented co-segregation with Mo and Cr at GBs, this raises the possibility of a synergistic effect in Ni-based alloys, where B and Mo together could provide an effective barrier against H embrittlement. The E_{excess} analysis provides intriguing support for this hypothesis, as B exhibited a strong segregation tendency with Mo. This suggests that, in Ni-based systems, GBs enriched in B and Mo could form highly resistant interfaces, where Mo-based borides play a critical role in repelling H and collectively mitigating HE. If such an effect extends to B-Mo-rich GBs in Inconel alloys, it would present a new alloy design strategy for improving H resistance. Specifically, the observed energetic preference for B and Mo to segregate together implies that engineering GB compositions to promote MoB boride formation could create self-stabilizing, H-resistant interfaces, preventing embrittlement and extending alloy performance in H-exposed environments.

Attention now shifts to N, the final light interstitial. Similar to C, N exhibited no solubility in the Ni lattice even in the presence of Cr, consistent with experimental data and phase equilibria studies [90–92]. These results further confirm the limited capacity of the $Cr_{30}Ni$ matrix to accommodate N in solid solution under the simulated conditions. Like the other light interstitials, N showed a strong preference for Nb and Ti. The shared affinity of C and N with Nb provides further support to the hypothesis that Nb competes in carbide and nitride formation in Ni superalloys [93]. Referencing Fig. 3a, N clearly demonstrated an extreme chemical affinity for Ti, with significantly higher E_{excess} values than any other light interstitial. This suggests that TiN formation is not only thermodynamically favorable but also a dominant segregation pathway for N, far outweighing its interactions with Cr or Mo. Experimental observations strongly support this trend, with TiN inclusions readily forming in Ni-based alloys and playing a critical role in nitrogen stabilization [21,22]. Both studies demonstrated that TiN remains thermodynamically stable under extreme processing conditions, reinforcing that Ti–N bonding is one of the strongest interstitial-metal interactions in Ni-based systems. However, while TiN formation is energetically favorable, its impact on mechanical properties must be carefully considered. The incorporation of TiN has been shown to enhance tensile strength and wear resistance, yet excessive TiN content leads to particle agglomeration, increasing embrittlement and reducing ductility [21]. Additionally, TiN was found to modify GB chemistry by reducing Laves phase formation and promoting a Nb-Mo diffusion layer at the TiN/IN718 interface. This is particularly noteworthy given that E_{excess} analysis indicated an affinity between N and Mo. Given the extreme chemical affinity between Ti and N, TiN precipitation is virtually unavoidable in N-bearing Ni-based alloys. These findings underscore the need for precise N content control in alloy design, especially in additively manufactured Inconel systems, where unintended N incorporation could lead to excessive TiN formation and associated mechanical degradation.

3.3. Grain boundary analysis

The data in Table 2 highlights the effect of increasing interstitial content on the free volume ($V_{\mathrm{GB}} - \langle V_{\mathrm{bulk}} \rangle$) of metallic atoms in the GB. At 1 at.% doping, all interstitials reduced the GB free volume relative to the undoped system ($\mu = 3.20\%$), with B exhibiting the most significant reduction ($\mu = 1.62\%$, $x_{\mathrm{GB}}^{(i)} = 3.09\%$). This was followed by H ($\mu = 1.91\%$, $x_{\mathrm{GB}}^{(i)} = 3.10\%$), C ($\mu = 2.14\%$, $x_{\mathrm{GB}}^{(i)} = 4.00\%$), then N ($\mu = 2.20\%$, $x_{\mathrm{GB}}^{(i)} = 4.62\%$). These values suggest that B was the most effective in densifying the GB and enhancing cohesion, while H exhibited the highest standard deviation ($\sigma = 4.75\%$), indicating that it introduced local structural variability within the GB. The reduction in free volume results from interstitial segregation to the GB, where they occupy previously unoccupied voids. At 2 at.% and 4 at.% doping, interstitials continued to fill the GB, with H showing the largest reduction in free volume and highest structural variability. This corresponded to an increase in $x_{\mathrm{GB}}^{(i)}$ for all species, indicating greater interstitial enrichment in the GB region at higher concentrations, with B having the highest interstitial content at the GB. Unlike B and H, which further reduced GB free volume, C and N showed diminishing effects, suggesting that their densification tendencies may saturate beyond a certain concentration. Increased standard deviations at higher interstitial contents, particularly for B and H at 4 at.%, indicate localized structural distortions. The H-doped GB structure at 4 at.% exhibited the most negative free volume ($\mu = -1.18\%$) and highest variability ($\sigma = 6.09\%$). This suggests that at high H concentrations, the GB undergoes pronounced compaction, which may also introduce localized stress concentrations. Such behavior aligns intuitively with H's small atomic radius, high diffusivity, and balanced chemical affinity for both Cr and Ni in the CrNi lattice. Considering surface roughness, negative values indicate that the doped GB planes were smoother than the undoped GB plane, demonstrating that light interstitials improved GB smoothness as they filled the voids between the metallic constituents, promoting a reduction in the γ_{GB}. Among the dopants, B produced the flattest planes at all dopant concentrations (most negative values), which corresponded to a continual decrease in γ_{GB} with increasing B content (see Fig. 4c). This suggests B improves cohesion among the GB constituents. Notably, there is a correlation between R_q and γ_{GB}, where rougher surfaces exhibited higher γ_{GB}. Consider the case for 2 at.% H, where the increased roughness ($\tilde{R}_q = 0.583$) corresponded to a γ_{GB} value that exceeded $\gamma_{\mathrm{GB}}^{(\mathrm{undoped})}$. This analysis highlights that all interstitials reduced GB free volume and smoothed the GB plane (with 2 at.% H as the exception). Among the light interstitials, B and H were the most effective at compacting the GB with increasing concentration, whereas C and N showed diminishing effects at higher concentrations, suggesting a rapid saturation of their GB stabilization influence.

The most significant findings from the GB simulations are compiled in Fig. 4. To begin, Fig. 4a presents the undoped GB simulation cell as visualized in OVITO with the grain segmentation modification applied. The atomic composition was analyzed layer-by-layer along the z-axis (visualized in Fig. S2c) to highlight GB segregation per species and is given in Fig. 4b. In the undoped system, a Cr enrichment peak (orange curve) appears in the central GB region (near 22.5 Å) and at the periodic boundary condition (PBC) GB (0 and 38 Å), indicating that Cr preferentially segregated to the GB. This Cr segregation trend was consistently observed in all doped systems. Additionally, in the doped systems interstitial segregation peaks (blue curves) were found around 20 Å in the central GB and at 0 and 38 Å at the PBC GB, confirming that light interstitials preferentially segregated to the GB. The peaks in Cr and interstitial content correspond to troughs in Ni content (green curves), indicating a redistribution of atomic species near the GB. However, in the H-doped cell, the inverse correlation between Cr and Ni is considerably less pronounced. This behavior aligns with the SRO results, which demonstrated that H had an affinity for both Cr and Ni, thereby reducing Ni migration away from the GB. As a result, H promoted Ni enrichment in regions that would otherwise experience Ni depletion. This altered chemical ordering could serve as an early-stage mechanism for GB decohesion. Furthermore, in the undoped and H-doped system, the central GB location migrated upwards from the initial placement around 20 Å to between 21 and 22.5 Å, respectively. This indicates that H had a limited impact on GB migration, despite producing a large impact on GB morphology (from Table 2). In the C- and N-doped systems, no significant migration occurred, indicating the formation of more rigid clusters. Meanwhile, in the B-doped system, there was a small migration downwards, toward 19 Å, as a result of B's ability to produce a smoother GB plane, effectively 'flattening' the GB structure.

The energetics of the GB simulation cells are presented in Fig. 4c, where the top figure shows γ_{GB} as a function of interstitial content and the bottom figure depicts E_{seg} versus interstitial content. Due to the symmetry in the way these values are calculated, similar trends appear in both plots, though they offer distinct insights. For B, C, and N, there was reduction in γ_{GB} relative to the undoped value of 0.800 J/m^2, suggesting that the segregation of these light elements into previously unoccupied voids stabilized the overall GB structure. The magnitude of this stabilization varied depending on the species, with B exhibiting the strongest stabilizing effect, as it continually decreased γ_{GB} as it filled the GB zone. Boron also had the lowest segregation energy, indicating that it is the most effective GB segregator in terms of thermal stability and the most likely to preferentially segregate among the interstitials considered. Unlike the other elements, B's impact on segregation and stabilization did not saturate up to 4 at.% total dopant concentration; the GB continued to stabilize as increasing amounts of B occupied the boundary region. Following B, C exhibited stabilization and segregation effects that quickly saturated beyond 2 at.%, indicating a critical trade-off in C segregation at the GB. Excessive C content could potentially destabilize the GB in the absence of alternate segregation pathways, such as carbide precipitation. Nitrogen showed an even faster saturation than C, with a noticeable increase in γ_{GB} and E_{seg} from 1 at.% to 4 at.%. This suggests that excessive N accumulation in the GB zone would eventually compromise the structural stability of the GB. Lastly, H exhibited relatively consistent behavior from 1 at.% to 4 at.%, with a notable increase in γ_{GB} at 2 at.%. This increase is attributed to reduced cohesion among metallic constituents, likely driven by increased structural variability and GB surface roughness (see

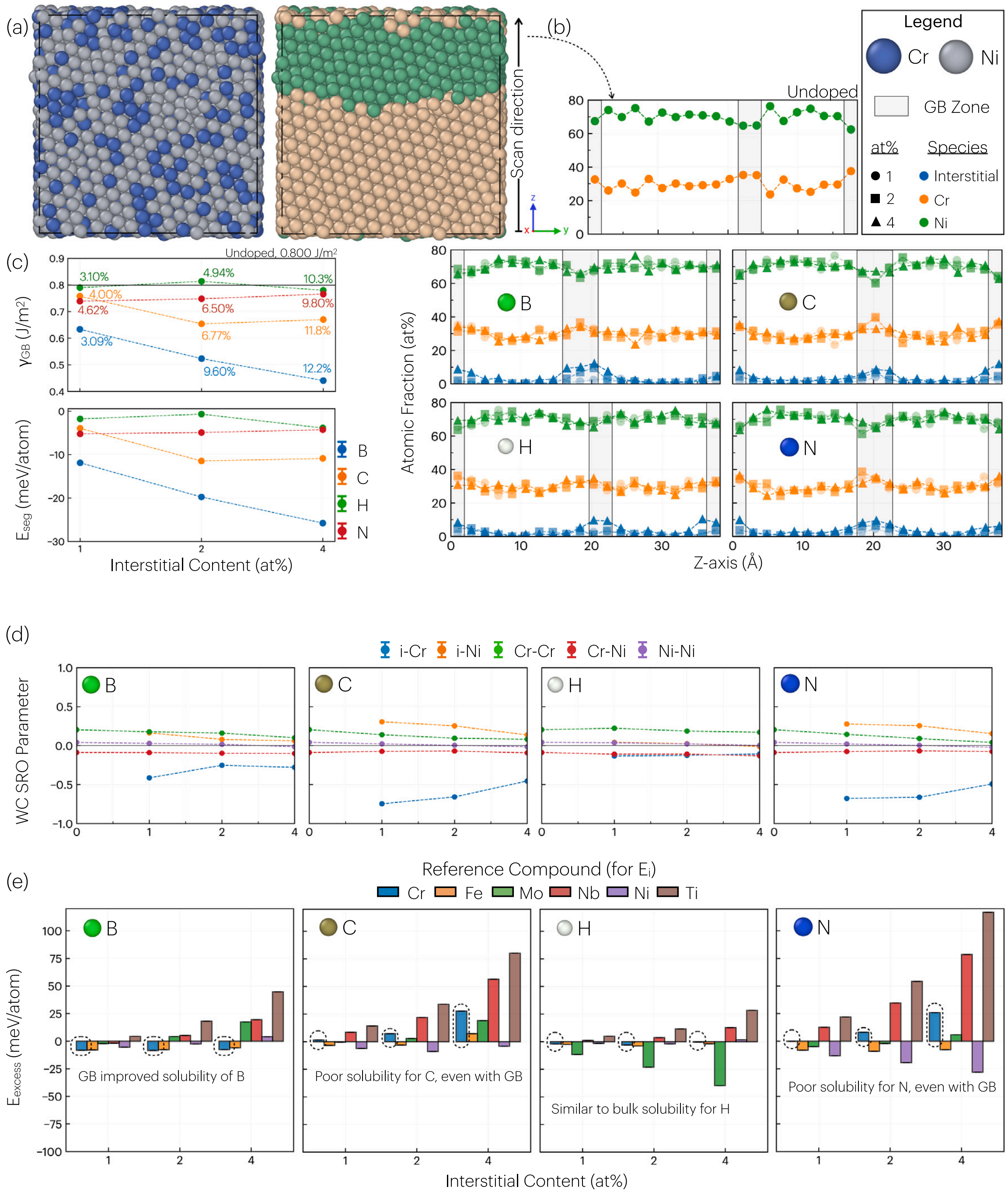

Fig. 4. (a) The undoped $Cr_{30}Ni$ grain boundary (GB) simulation cell, shown without and with the grain segmentation modification applied in OVITO. (b) The atomic composition of the equilibrated GB simulation cells as a function of the z-axis. Colors distinguish chemical species, while marker symbols indicate different dopant concentrations. (c) The GB energy (γ_{GB}) and segregation energy (E_{seg}) as a function of interstitial content. For better reference, the interstitial content *in the GB zone* is annotated near the corresponding γ_{GB} value. (d) The SRO parameter (α_{ij}) plotted as a function of interstitial content. (e) The excess energy (E_{excess}) plotted as a function of interstitial content and reference compound used for interstitial chemical potential energy (E_i).

Table 2). Since the MC routine equilibrated the system to its thermodynamically preferred state, the high concentration of H within the GB zone confirms its strong preference for the GB environment. However, despite this preference, the energetic benefit of H segregation remained minimal or deleterious, resulting in geometric disorder, which is likely to drive the system toward a state prone to embrittlement.

The SRO results for the GB simulation cell are presented in Fig. 4d. Co-segregation of Cr and light interstitials to the GB region resulted in negative α_{iCr} values, indicating a strong local preference for Cr. Similar to the bulk system, C and N exhibited the strongest affinity for Cr, further enriching the GB region with Cr as they segregated. This is reflected in the lower α_{CrCr} values with increased C and N content. Additionally, the M-M' α_{ij} values for Cr–Ni and Cr-Cr decreased in the undoped GB system relative to the undoped pristine system, suggesting that the GB environment altered the preferred atomic ordering. These insights highlight the dual influence of chemical composition and geometric constraints in shaping SRO behavior, demonstrating that atomic ordering is governed not only by elemental interactions but also by the spatial configuration offered in the GB.

The excess energy results are presented in Fig. 4e, showing a small increase in the number of negative values compared to those reported for bulk $Cr_{30}Ni$. Combined with the bulk predictions, these results provide a more comprehensive understanding of the segregation and precipitation tendencies of light interstitials. For example, B previously exhibited a strong tendency to leave the $Cr_{30}Ni$ lattice (see Fig. 3b). However, when given the opportunity to segregate to the GB, B no longer exhibits an energetic preference to 'escape' the simulation cell. Even as more B accumulated within the GB zone, its B-Cr excess energy remained largely unchanged, indicating strong solubility of B in the Cr–Ni GB. Notably, the likelihood of B segregation increased in the presence of Mo, Nb, and Ti. This suggests that the chemical affinity of B for these elements, combined with its GB solubility, may lead to the enrichment of Mo, Nb, and/or Ti around B-doped GBs. Together with the bulk insights, the excess energy and GB energetics confirm that B not only exhibits a thermodynamic preference to leave the bulk lattice but also demonstrates a strong segregation tendency toward GBs. Among all the light interstitials considered in this study, B shows the highest GB enrichment and the most pronounced stabilization effect. This behavior suggests that B does not favor the formation of precipitates or secondary phases within the microstructure; instead, it preferentially segregates to GBs, where it plays a critical role in enhancing cohesion and reducing the GB energy. As such, B can be classified as the most potent GB stabilizer among the light interstitials evaluated here.

Meanwhile, C and N exhibit distinct behavior, showing a preference to associate with Cr rather than remain uniformly distributed within the $Cr_{30}Ni$ GB simulation cell. This prediction aligns well with established experimental observations that C and N tend to form stable carbides or nitrides, rather than remain dissolved within the GB region [80–82,93]. As the concentrations of C and N increased within the GB zone, the probability of Cr–(C,N) association also increased, reinforcing the likelihood of Cr-based carbide and nitride formation under such conditions. For H, its segregation behavior showed minimal deviation from the bulk E_{excess} values. However, the MC routine confirmed that H aggregation at the GB is thermodynamically preferred. Since H is typically introduced into the material through environmental exposure, GBs would have already formed prior to significant H ingress. These findings suggest that H preferentially migrates along GB channels rich in Cr and Ni, while the increasingly negative E_{excess} values for H-Mo indicate a strong tendency for H to avoid Mo-enriched GBs. This is consistent with the repulsive interactions observed in both the GB and bulk environments (see Fig. 3b) and aligns with recent studies highlighting Mo's role in mitigating HE [32,84–86]. Alternatively, increased Nb or Ti concentrations at the GB appear to facilitate H diffusion, though to a lesser extent than Mo's repulsive effect. This segregation behavior could have important implications for HE mechanisms, particularly in service environments where H ingress is a concern.

4. Conclusion

This study systematically investigated the behavior of light interstitials (B, C, H, and N) in a $Cr_{30}Ni$ alloy, considering both bulk and grain boundary (GB) environments. Through Monte Carlo simulations, we identified clear chemical and geometric preferences for each interstitial, providing atomistic insights corroborated to experimentally observed segregation and precipitation trends in Ni-based superalloys.

A key finding of this study was boron's strong preference to leave the bulk lattice and segregate to GBs. Once in the GBs, B had the most pronounced effect, where it reduced the GB energy and promoted a more cohesive GB. This aligned well with experimental observations that report B's role in enhancing GB cohesion which promotes exceptional creep resistance at high temperatures. Interestingly, B was the only light interstitial to induce a structural transformation in the bulk, disrupting the original ordering and indicating a strong driving force for segregation. Upon removing B and re-relaxing the system, the metal lattice largely reverted to its primary FCC structure. This behavior aligns with B's experimentally observed role in promoting serrated GBs, which are known to enhance resistance to GB sliding and improve high-temperature mechanical properties. These atomistic insights reinforce the well-established understanding that B primarily acts as a GB strengthening element rather than driving bulk precipitation. In contrast, carbon and nitrogen exhibited strong ordering with Cr in both bulk and GB environments, forming carbide- and nitride-like motifs consistent with experimentally observed precipitation behavior in high-temperature alloys. Additionally, their solubility within the Cr–Ni GB was limited, instead preferring to segregate with Cr over remaining dissolved in the GB. This aligns with experimental observations of carbide and nitride precipitation rather than a homogeneous distribution. Importantly, the shared chemical affinities and GB segregation tendencies of B, C, and N highlight the potential for complex multi-element interactions, including the formation of mixed boro-nitro-carbides, borocarbides, and carbonitrides. These interactions could further influence microstructural stability and mechanical performance.

Hydrogen exhibited strong aggregation within the GB structure, suggesting that Cr–Ni GBs may serve as diffusion pathways for H ingress. Unlike other light interstitials, H segregation did not enhance GB stability but instead introduced additional atomic disorder. This finding aligns with experimental studies on hydrogen embrittlement in Ni-based alloys, where H-induced decohesion frequently occurs along GBs. Additionally, H was found to avoid ordering with Mo, supporting recent findings on Mo's role in mitigating embrittlement. The repulsion of H from Mo-rich regions in both bulk and GB environments further reinforces mechanistic explanations of Mo segregation enhancing embrittlement resistance.

Based on our findings, we propose the following hypothesis to the community for future analysis (also illustrated in Fig. 1):

- Mo-containing borides act as effective barriers against hydrogen-induced degradation by inhibiting H ingress and stabilizing GB cohesion.

By elucidating both the chemical and structural preferences of these interstitials—specifically their metallic ordering and bulk vs. GB occupancy—our work provides a robust computational framework for interpreting experimental segregation studies. This level of predictive insight is critical for designing next-generation superalloys with improved GB stability, enhanced resistance to embrittlement, and optimized precipitation behavior. Future work will extend these findings by incorporating additional alloying elements and exploring kinetic effects on interstitial diffusion and clustering.

CRediT authorship contribution statement

Tyler D. Doležal: Writing – review & editing, Writing – original draft, Visualization, Validation, Methodology, Investigation, Formal analysis, Data curation, Conceptualization. **Rodrigo Freitas:** Writing – review & editing, Validation, Supervision, Project administration. **Ju Li:** Supervision, Software, Resources, Project administration, Funding acquisition.

Declaration of competing interest

The authors declare that they have no known competing financial interests or personal relationships that could have appeared to influence the work reported in this paper.

Acknowledgments

J. Li acknowledges support from National Science Foundation, USA CMMI-1922206 and DMR-1923976.

Appendix A. Supplementary data

Supplementary material related to this article can be found online at https://doi.org/10.1016/j.actamat.2025.121221.

Data availability

The hybrid Monte Carlo Molecular Dynamics (hMCMD) routine will be made available at https://github.com/tylerdolezal/hybrid_MCMD. All data generated from this work and post-processing scripts will be provided at https://github.com/tylerdolezal.

References

[1] E. Hosseini, V.A. Popovich, A review of mechanical properties of additively manufactured Inconel 718, Addit. Manuf. 30 (2019) 100877.

[2] Q. Jia, D. Gu, Selective laser melting additive manufacturing of Inconel 718 superalloy parts: Densification, microstructure, and properties, J. Alloys Compd. 585 (2014) 713–721.

[3] I.F.M. de Souza, K.C. Riffel, L.E. dos Santos Paes, S.D. Franco, L.R.R. da Silva, Welding and additive manufacturing challenges in nickel superalloys: The impact of hydrogen embrittlement, Processes 13 (1) (2025) 33.

[4] M.C. Hardy, M. Detrois, E.T. McDevitt, C. Argyrakis, V. Saraf, P.D. Jablonski, J.A. Hawk, R.C. Buckingham, H.S. Kitaguchi, S. Tin, Solving recent challenges for wrought Ni-base superalloys, Met. Mater. Trans. A 51 (6) (2020) 2626–2650.

[5] H. Khalid, B. Mansoor, Hydrogen embrittlement in nickel-base superalloy 718, in: I. ulhaq Toor (Ed.), Recent Developments in Analytical Techniques for Corrosion Research, Springer International Publishing, Cham, 2022, pp. 279–306.

[6] J. Feng, X. Zhang, Y. Chu, J. Wan, Hydrogen embrittlement of Ni-based superalloy inconel 625 fabricated by wire arc additive manufacturing: the role of laves phase, Met. Mater. Int. 30 (4) (2024) 872–885.

[7] S.-H. Baek, S. He, M.-S. Jang, D.-H. Back, D.-W. Jeong, S.-H. Park, Ultrasonic nanocrystal surface modification effect on reduction of hydrogen embrittlement in Inconel-625 parts fabricated via additive manufacturing process, J. Manuf. Process. 108 (2023) 685–695.

[8] Z. Fu, P. Wu, Y. Zhang, K. Gan, D. Yan, Z. Li, Effects of hydrogen and load frequency on the fatigue crack propagation behavior of selective laser melted Inconel 718 alloy, Int. J. Fatigue 160 (2022) 106848.

[9] J. Xu, Z. Hao, Z. Fu, X. He, H. Wang, G. Xu, Hydrogen embrittlement behavior of selective laser-melted Inconel 718 alloy, J. Mater. Res. Technol. 23 (2023) 359–369.

[10] D.-H. Lee, Y. Zhao, S.Y. Lee, D. Ponge, E.A. Jägle, Hydrogen-assisted failure in Inconel 718 fabricated by laser powder bed fusion: The role of solidification substructure in the embrittlement, Scr. Mater. 207 (2022) 114308.

[11] S. Antonov, A. Després, C. Mayer, G. Martin, P. Kontis, Boron trapping at dislocations in an additively manufactured polycrystalline superalloy, Materialia 30 (2023) 101801.

[12] P. Kontis, H.A. Mohd Yusof, K. Moore, C. Grovenor, R. Reed, On the effect of boron on the mechanical properties of a new polycrystalline superalloy, MATEC Web Conf. 14 (2014) 17003.

[13] P.-J. Zhou, J. Yu, X. Sun, H. Guan, Z. Hu, The role of boron on a conventional nickel-based superalloy, Mater. Sci. Eng. A- Struct. Mater. Prop. Microstruct. Process. - Mater. Sci. Eng. A.- Struct. Mater. 491 (2008) 159–163.

[14] B. Zhang, G. Bi, S. Nai, C.-n. Sun, J. Wei, Microhardness and microstructure evolution of TiB2 reinforced Inconel 625/TiB2 composite produced by selective laser melting, Opt. Laser Technol. 80 (2016) 186–195.

[15] Q. Tian, S. Huang, H. Qin, R. Duan, C. Wang, X. Lian, Synergistic effects of boron and rare earth elements on the microstructure and stress rupture properties in a Ni-based superalloy, Materials 17 (9) (2024) 2007.

[16] E. Tekoğlu, A.D. O'Brien, J. Liu, B. Wang, S. Kavak, Y. Zhang, S.Y. Kim, S. Wang, D. Ağaoğulları, W. Chen, A.J. Hart, J. Li, Strengthening additively manufactured Inconel 718 through in-situ formation of nanocarbides and silicides, Addit. Manuf. 67 (2023) 103478.

[17] W. Liu, B. Zou, X. Wang, S. Ding, J. Liu, L. Li, C. Huang, P. Yao, Tailored microstructure and enhanced high temperature behavior of TiC/Inconel 718 composites through dual-gradient printing strategy in direct energy deposition, J. Mater. Process. Technol. 336 (2025) 118679.

[18] C. Zhao, Y. Zhou, X. Xing, S. Liu, X. Ren, Q. Yang, Precipitation stability and micro-property of (Nb, Ti)C carbides in MMC coating, J. Alloys Compd. 763 (2018) 670–678.

[19] C. Guan, Y. Chen, F. Meng, L. Chen, Z. Ma, T. Yu, Microstructure and mechanical properties of in-situ TiB2/TiC/(Ti, Nb)C reinforced Inconel 718 coating by laser direct energy deposition, Mater. Charact. 220 (2025) 114709.

[20] Y.I. Kim, H.S. Chung, W.W. Kim, J.S. Kim, W.J. Lee, A study on pitting corrosion of TiN-coated inconel 600 by immersion test in high temperature chloride solutions, Surf. Coat. Technol. 80 (1) (1996) 113–116.

[21] Y. Li, H. Yan, B. Zhang, P. Zhang, H. Shi, Q. Lu, Investigating the influence of TiN on microstructural, mechanical, and tribological properties in selective laser melting of Inconel 718-based composites, Mater. Today Commun. 40 (2024) 110075.

[22] K.-H. Lim, K. Ryou, J.-H. Choi, G. Choi, W.S. Choi, J.-H. Lee, C.-S. Oh, P.-P. Choi, G.-D. Sim, Effect of titanium nitride inclusions on the mechanical properties of direct laser deposited Inconel 718, Extrem. Mech. Lett. 61 (2023) 102009.

[23] J. yuan Ji, Z. Zhang, J. Chen, H. Zhang, Y.Z. Zhang, H. Lu, Effect of refractory elements M (=Re, W, Mo or Ta) on the diffusion properties of boron in nickel-based single crystal superalloys, Vacuum 211 (2023) 111923.

[24] Z. Rák, C.J. O'Brien, D.W. Brenner, First-principles investigation of boron defects in nickel ferrite spinel, J. Nucl. Mater. 452 (1) (2014) 446–452.

[25] J. Yang, J. Huang, D. Fan, S. Chen, X. Zhao, First-principles investigation on the interaction of boron atom with nickel part I: from surface adsorption to bulk diffusion, J. Alloys Compd. 663 (2016) 116–122.

[26] J. Yang, J. Huang, Z. Ye, D. Fan, S. Chen, Y. Zhao, First-principles investigation on the interaction of boron atom with nickel part II: absorption and diffusion at grain boundary, J. Alloys Compd. 708 (2017) 1089–1095.

[27] C. Yu, T. Kawabata, T. Okita, S. Uranaka, First-principles study of hydrogen solubility and embrittlement of Cr23C6 in nickel-based alloys, Comput. Mater. Sci. 245 (2024) 113304.

[28] X. Hu, T. Björkman, H. Lipsanen, L. Sun, A.V. Krasheninnikov, Solubility of boron, carbon, and nitrogen in transition metals: getting insight into trends from first-principles calculations, J. Phys. Chem. Lett. 6 (16) (2015) 3263–3268.

[29] M. David, A. Prillieux, D. Monceau, D. Connétable, First-principles study of the insertion and diffusion of interstitial atoms (H, C, N and O) in nickel, J. Alloys Compd. 822 (2020) 153555.

[30] E. Tekoğlu, A.D. O'Brien, J.-S. Bae, K.-H. Lim, J. Liu, S. Kavak, Y. Zhang, S.Y. Kim, D. Ağaoğulları, W. Chen, A.J. Hart, G.-D. Sim, J. Li, Metal matrix composite with superior ductility at 800 °C: 3D printed In718+ZrB2 by laser powder bed fusion, Compos. Part B: Eng. 268 (2024) 111052.

[31] Y. Chen, Z. Fu, J. Ye, B. Wahlmann, C. Körner, Additive manufacturing of TiC/Steel composites using electron beam melting and in situ infiltration, Adv. Eng. Mater. 26 (9) (2024) 2301313.

[32] J. Lee, T. Lee, D.-J. Mun, C.M. Bae, C.S. Lee, Comparative study on the effects of Cr, V, and Mo carbides for hydrogen-embrittlement resistance of tempered martensitic steel, Sci. Rep. 9 (1) (2019) 5219.

[33] P. Hirel, Atomsk: A tool for manipulating and converting atomic data files, Comput. Phys. Comm. 197 (2015) 212–219.

[34] A.P. Thompson, H.M. Aktulga, R. Berger, D.S. Bolintineanu, W.M. Brown, P.S. Crozier, P.J. in 't Veld, A. Kohlmeyer, S.G. Moore, T.D. Nguyen, R. Shan, M.J. Stevens, J. Tranchida, C. Trott, S.J. Plimpton, LAMMPS - a flexible simulation tool for particle-based materials modeling at the atomic, meso, and continuum scales, Comput. Phys. Comm. 271 (2022) 108171.

[35] S. Takamoto, C. Shinagawa, D. Motoki, K. Nakago, W. Li, I. Kurata, T. Watanabe, Y. Yayama, H. Iriguchi, Y. Asano, T. Onodera, T. Ishii, T. Kudo, H. Ono, R. Sawada, R. Ishitani, M. Ong, T. Yamaguchi, T. Kataoka, A. Hayashi, N. Charoenphakdee, T. Ibuka, Towards universal neural network potential for material discovery applicable to arbitrary combination of 45 elements, Nat. Commun. 13 (1) (2022) 2991.

[36] Matlantis, Software as a Service Style Material Discovery Tool, https://matlantis.com/.

[37] G.S. Rohrer, E.A. Holm, A.D. Rollett, S.M. Foiles, J. Li, D.L. Olmsted, Comparing calculated and measured grain boundary energies in nickel, Acta Mater. 58 (15) (2010) 5063–5069.

[38] M.D. Sangid, H. Sehitoglu, H.J. Maier, T. Niendorf, Grain boundary characterization and energetics of superalloys, Mater. Sci. Eng.: A 527 (26) (2010) 7115–7125.

[39] N. Metropolis, A.W. Rosenbluth, M.N. Rosenbluth, A.H. Teller, E. Teller, Equation of state calculations by fast computing machines, J. Chem. Phys. 21 (1953) 1087–1092.

[40] S. Mine, T. Toyao, K.-i. Shimizu, Y. Hinuma, Comparison of matlantis and VASP bulk formation and surface energies in metal hydrides, carbides, nitrides, oxides, and sulfides, 2023.

[41] T. Kato, F. Lodesani, S. Urata, Boron coordination and three-membered ring formation in sodium borate glasses: A machine-learning molecular dynamics study, J. Am. Ceram. Soc. 107 (5) (2024) 2888–2900.

[42] S. Choung, W. Park, J. Moon, J.W. Han, Rise of machine learning potentials in heterogeneous catalysis: developments, applications, and prospects, Chem. Eng. J. 494 (2024) 152757.

[43] K. Hisama, K.V. Bets, N. Gupta, R. Yoshikawa, Y. Zheng, S. Wang, M. Liu, R. Xiang, K. Otsuka, S. Chiashi, B.I. Yakobson, S. Maruyama, Molecular dynamics of catalyst-free edge elongation of boron nitride nanotubes coaxially grown on single-walled carbon nanotubes, ACS Nano 18 (45) (2024) 31586–31595.

[44] Y. Hinuma, Neural network potential molecular dynamics simulations of (La,Ce,Pr,Nd)0.95(Mg,Zn,Pb,Cd,Ca,Sr,Ba)0.05F2.95, J. Phys. Chem. B 128 (49) (2024) 12171–12178.

[45] J.M. Cowley, An approximate theory of order in alloys, Phys. Rev. 77 (5) (1950) 669–675.

[46] J.M. Cowley, Short- and long-range order parameters in disordered solid solutions, Phys. Rev. 120 (5) (1960) 1648–1657.

[47] P.M. Larsen, S. Schmidt, J. Schiøtz, Robust structural identification via polyhedral template matching, Modelling Simul. Mater. Sci. Eng. 24 (5) (2016) 055007.

[48] A. Stukowski, Visualization and analysis of atomistic simulation data with OVITO–the open visualization tool, Modelling Simul. Mater. Sci. Eng. 18 (1) (2009) 015012.

[49] A. Jain, S.P. Ong, G. Hautier, W. Chen, W.D. Richards, S. Dacek, S. Cholia, D. Gunter, D. Skinner, G. Ceder, K.A. Persson, Commentary: the materials project: A materials genome approach to accelerating materials innovation, APL Mater. 1 (1) (2013) 011002.

[50] P. Lejcek, Grain Boundary Segregation in Metals, in: Springer Series in Materials Science, vol. 136, Springer, Berlin, Heidelberg, 2010.

[51] Y. Niu, X. Huang, Y. Wang, M. Xu, J. Chen, S. Xu, M.-G. Willinger, W. Zhang, M. Wei, B. Zhang, Manipulating interstitial carbon atoms in the nickel octahedral site for highly efficient hydrogenation of alkyne, Nat. Commun. 11 (1) (2020) 3324.

[52] Q. Wang, Y. Wu, J. Chen, J. Song, C. Xiao, X. Hui, Insight into the low cycle fatigue deformation mechanisms of minor element doping single crystal superalloys at elevated temperature, Scr. Mater. 224 (2023) 115151.

[53] L. Zhang, Q. Yang, J. Chen, M. Zhang, C. Xiao, Synergy of γ' phase, MC carbide and grain boundary phase on creep behavior for nickel-based superalloy K439B, Mater. Sci. Eng.: A 915 (2024) 147261.

[54] R. Li, Y. Zhang, H. Niu, H. Wang, H. Wu, Influence of carbides and pores on the localized deformation of nickel-based single-crystal superalloys, Prog. Nat. Sci.: Mater. Int. 34 (3) (2024) 562–568.

[55] B. Nabavi, M. Goodarzi, A.K. Khan, Metallurgical effects of nitrogen on the microstructure and hot corrosion behavior of alloy 718 weldment, Mater. Charact. 157 (2019) 109916.

[56] A.K. Koul, G.H. Gessinger, On the mechanism of serrated grain boundary formation in Ni-based superalloys, Acta Metall. 31 (7) (1983) 1061–1069.

[57] H. Danflou, M. Marty, A. Walder, Formation of serrated grain boundaries and their effect on the mechanical properties in a P/M nickel base superalloy, in: Superalloys 1992 Seventh International Symposium, TMS, 1992, pp. 63–72.

[58] P. Kontis, E. Alabort, D. Barba, D.M. Collins, A.J. Wilkinson, R.C. Reed, On the role of boron on improving ductility in a new polycrystalline superalloy, Acta Mater. 124 (2017) 489–500.

[59] W.H. Philipp, Stability of Titanium Nitride and Titanium Carbide When Exposed to Hydrogen Atoms from 298 to 1950 K, Tech. Rep. E-1291, NASA, 1961.

[60] W.H. Philipp, Chemical Reactions of Carbides, Nitrides, and Diborides of Titanium and Zirconium and Chemical Bonding in These Compounds, Tech. Rep. NASA-TN-D-3533, NASA, 1966.

[61] H.O. Pierson, Handbook of Refractory Carbides and Nitrides: Properties, Characteristics, Processing and Applications, William Andrew, 1996.

[62] Q. Gu, G. Krauss, W. Steurer, Transition metal borides: superhard versus ultra-incompressible, Adv. Mater. 20 (19) (2008) 3620–3626.

[63] D. Setoyama, J. Matsunaga, H. Muta, M. Uno, S. Yamanaka, Mechanical properties of titanium hydride, J. Alloys Compd. 381 (1) (2004) 215–220.

[64] L. Luo, Y. Su, J. Guo, H. Fu, Formation of titanium hydride in Ti–6Al–4V alloy, J. Alloys Compd. 425 (1) (2006) 140–144.

[65] J.J. Xu, H.Y. Cheung, S.Q. Shi, Mechanical properties of titanium hydride, J. Alloys Compd. 436 (1) (2007) 82–85.

[66] A. Friedrich, B. Winkler, E.A. Juarez-Arellano, L. Bayarjargal, Synthesis of binary transition metal nitrides, carbides and borides from the elements in the laser-heated diamond anvil cell and their structure-property relations, Materials 4 (10) (2011) 1648–1692.

[67] K.I. Portnoi, V.M. Romashov, V.M. Chubarov, M.K. Levinskaya, S.E. Salibekov, Phase diagram of the system nickel-boron, Sov. Powder Met. Met. Ceram. 6 (2) (1967) 99–103.

[68] P.K. Liao, K.E. Spear, The B-Cr (boron-chromium) system, Bull. Alloy. Phase Diagr. 7 (3) (1986) 232–237.

[69] K. Oikawa, N. Ueshima, Experimental investigation and thermodynamic assessment of Ni–B and Ni–B–C systems, J. Phase Equilib. Diffus. 43 (6) (2022) 814–826.

[70] E. Tekoglu, J.-S. Bae, H.-A. Kim, K.-H. Lim, J. Liu, T. Doležal, S. Kim, M. Alrizqi, A. Penn, W. Chen, A. Hart, J.-H. Kang, C.-S. Oh, J. Park, F. Sun, S. Kim, G.-D. Sim, J. Li, Superior high-temperature mechanical properties and microstructural features of LPBF-printed in625-based metal matrix composites, Mater. Today 80 (2024) 297–307.

[71] Z. Wang, C. Liang, X. Ding, D. Wang, New insights into the partitioning behavior of Mo in nickel-based superalloys and its effect on microstructure using CALPHAD-assisted phase field modeling, Acta Mater. 282 (2025) 120510.

[72] X.G. Liu, L. Wang, L.H. Lou, J. Zhang, Effect of mo addition on microstructural characteristics in a re-containing single crystal superalloy, J. Mater. Sci. Technol. 31 (2) (2015) 143–147.

[73] B. Wang, J. Zhang, T. Huang, H. Su, Z. Li, L. Liu, H. Fu, Influence of W, Re, Cr, and Mo on microstructural stability of the third generation Ni-based single crystal superalloys, J. Mater. Res. 31 (21) (2016) 3381–3389.

[74] Z. Ma, Y.-L. Pei, L. Luo, L. Qin, S.-S. Li, S.-K. Gong, Partitioning behavior and lattice misfit of γ/Γ' phases in Ni-based superalloys with different Mo additions, Rare Met. 40 (4) (2021) 920–927.

[75] M. Singleton, P. Nash, The C-Ni (carbon-nickel) system, Bull. Alloy. Phase Diagr. 10 (2) (1989) 121–126.

[76] M. Venkatraman, J.P. Neumann, The C-Cr (carbon-chromium) system, Bull. Alloy. Phase Diagr. 11 (2) (1990) 152–159.

[77] H. Li, K. Reuter, Ab initio thermodynamic stability of carbide catalysts under electrochemical conditions, ACS Catal. 12 (16) (2022) 10506–10513.

[78] X. Xie, Y. Zeng, L. Kou, J. Dong, L. Pike, D. Klarstrom, The precipitation and strengthening behavior of Ni2(Mo,Cr) in HASTELLOY® C-22HS® alloy, a newly developed high molybdenum Ni-base superalloy, in: Proceedings of the International Symposium on Superalloys, 2008, p. 805.

[79] E. Cabrol, C. Bellot, P. Lamesle, D. Delagnes, E. Povoden-Karadeniz, Experimental investigation and thermodynamic modeling of molybdenum and vanadium-containing carbide hardened iron-based alloys, J. Alloys Compd. 556 (2013) 203–209.

[80] B. Bian, L. Söltzer, G.M. Muralikrishna, S. Taheriniya, S. Sen, K.C. Hari Kumar, S. S., G. Wilde, S.V. Divinski, Grain boundary diffusion in a compositionally complex alloy: interplay of segregation, precipitation and interface structures in a Ni–Cr–Mo alloy, Acta Mater. 269 (2024) 119803.

[81] L. Wei, B. Pan, Y. Wang, B. Li, X. Jia, Microstructure evolution and creep-rupture behaviour of a low-cost Fe-Ni-based superalloy, Mater. Technol. 38 (1) (2023) 2270865.

[82] S. Liu, X.-X. Ye, T. Wu, W. Yin, H. Chen, J. Xu, X. Zhou, Effects of Nb addition on the carbides, grain boundary characteristics and tensile properties of a Ni–26W–6Cr-based superalloy, Mater. Sci. Eng.: A 894 (2024) 146176.

[83] S. Li, X. Wang, C. Chen, Effect of annealing temperature on carbide precipitation, microstructure and mechanical properties of Fe-Mn-C- (Cr, Mo, W, Ni, Nb, Ti, V) multi-alloying TWIP steel, Mater. Today Commun. 39 (2024) 108895.

[84] J. Lee, T. Lee, Y.J. Kwon, D.-J. Mun, J.-Y. Yoo, C.S. Lee, Role of Mo/V carbides in hydrogen embrittlement of tempered martensitic steel, Corros. Rev. 33 (6) (2015) 433–441.

[85] J. Lee, T. Lee, Y.J. Kwon, D.-J. Mun, J.-Y. Yoo, C.S. Lee, Effects of vanadium carbides on hydrogen embrittlement of tempered martensitic steel, Met. Mater. Int. 22 (3) (2016) 364–372.

[86] L.C. Liu, Z.P. Wu, Z.Y. Xu, S.F. Zhou, Effects of W and Mo concentration on hydrogen embrittlement and elastic properties of V membrane, Int. J. Hydrog. Energy 89 (2024) 1105–1111.

[87] M. Eškinja, G. Winter, H. Schnideritsch, J. Klarner, V. Razumovskiy, M. Moshtaghi, G. Mori, Influence of Mo carbides and two-stage tempering methodology on the susceptibility of medium carbon martensitic steel to hydrogen embrittlement, Eng. Fail. Anal. 163 (2024) 108562.

[88] S.-G. Kim, H.-C. Shin, H.-G. Jung, B. Hwang, Hydrogen embrittlement behavior of tempered martensitic Ni–Cr–Mo low-alloy steel subjected to normalizing and annealing, Int. J. Hydrog. Energy 101 (2025) 1304–1311.

[89] G. Hachet, A. Tehranchi, H. Shi, M. Prabhakar, S. Wei, K. Angenendt, S. Zaefferer, B. Gault, B. Sun, D. Ponge, D. Raabe, Segregation at prior austenite grain boundaries: The competition between boron and hydrogen, Int. J. Hydrog. Energy 95 (2024) 734–746.

[90] C. Kowanda, M.O. Speidel, Solubility of nitrogen in liquid nickel and binary Ni–Xi alloys (Xi=Cr, Mo,W, Mn, Fe, Co) under elevated pressure, Scr. Mater. 48 (8) (2003) 1073–1078.

[91] X.-Z. Li, H.-B. Li, H. Feng, S.-X. Yang, S.-C. Zhang, H.-C. Zhu, Z.-H. Jiang, Nitrogen solubility in molten Ni, Ni-Cr, Ni-mo, and Ni-Cr-Mo alloys under pressurized atmosphere, Met. Mater. Trans. B 54 (1) (2023) 203–212.

[92] V.G. Ivanchenko, Phase equilibria and stability of the phase composition in chromium alloys with interstitial phases, Powder Met. Met. Ceram. 35 (7) (1996) 462–469.

[93] G. Smith, S. Patel, The role of niobium in wrought precipitation-hardened nickel-base alloys, Proc. Int. Symp. Superalloys Var. Deriv. (2005) 154.